Spectroscopic Studies of Cyclo-metallated Pt(II) Complexes: Optical Absorption and Emission and the Structure of Single Crystal $[Pt(bpm)(CN)_2]\cdot H_2O$ (bpm = 2,2′-bipyrimidine)

JOSEF BIEDERMANN, GÜNTER GLIEMANN*

Institut für Physikalische und Theoretische Chemie, Universität Regensburg, D-8400 Regensburg (F.R.G.)

ULRICH KLEMENT, KLAUS-JÜRGEN RANGE* and MANFRED ZABEL

Institut für Anorganische Chemie, Universität Regensburg, D-8400 Regensburg (F.R.G.)

(Received July 24, 1989)

Abstract

The polarized optical absorption and emission spectra of single crystal $[Pt(bpm)(CN)_2]\cdot H_2O$ (bpm = 2,2′-bipyrimidine) have been measured as functions of temperature (1.9 K $\leqslant T \leqslant$ 295 K) and of homogeneous magnetic fields ($0 \leqslant H \leqslant 6$ T). Analysis of the spectra shows that the inter-complex coupling is weak and that the emission at low temperatures originates mainly from two types of traps located energetically by $\Delta\bar{\nu} \sim 40$ and ~ 45 cm^{-1}, respectively, below the triplet exciton band. The spectroscopic properties are discussed on the basis of the crystallographic data for $[Pt(bpm)(CN)_2]\cdot H_2O$: monoclinic, space group $P2_1/c$, a = 7.076(1), b = 8.999(2), c = 18.127(2) Å, β = 99.84(1)°, V = 1137.29 Å^3, Z = 4, D_x = 2.47 g cm^{-3}. Anisotropic refinement (2743 reflexes $I > 2\sigma(I)$, 163 variables) resulted in R = 0.066, R_w = 0.037, S = 0.78.

Introduction

During recent years much attention has been given to the photophysical and photochemical properties of cyclo-metallated transition metal complexes [1–10]. In these systems the character of the lowest excited electronic states (LF, LC, MLCT or LMCT) depends on the type of the central metal and/or of the ligands. Sometimes even a substitution at the ligand [11–13] or a variation of the solvent changes this character distinctly [14, 15]. According to their electronic structure several cyclo-metallated transition metal complexes can be used as light emission sensitizers (LES), as light absorption sensitizers (LAS) or for the interconversion between light energy and chemical energy [1–8].

Recently we reported on the optical properties of single crystal $[Pt(CN)_2L]$ with L = *o*-phen or bipy as functions of the temperature and of applied magnetic fields [16, 17]. For these compounds the experimental results indicate a strong inter-complex coupling in the solid state causing a change from the LC type (glas) to the MLCT type (single crystal). This interesting feature gave rise to the present paper on single crystal $[Pt(bpm)(CN)_2]\cdot H_2O$. Unlike the ligands *o*-phen and bipy the molecule bpm can function as a twofold bidentate ligand bridging two central ions or, as in the present case, it can offer its two non-coordinating nitrogen atoms for the formation of hydrogen bonds. Thus, depending on the conditions of crystallization different crystal structures result. The different structures exhibit different inter-complex Pt–Pt distances yielding partly fundamental differences of the optical properties [18]. Single crystal $[Pt(bpm)(CN)_2]\cdot H_2O$ turns out to be a system of relatively largely separated complexes.

Experimental

The compound $[Pt(bpm)(CN)_2]\cdot H_2O$ was prepared according to ref. 19. Yellow needle shaped single crystals (size ~0.5 × 0.3 × 0.1 mm) were grown by slow cooling of a hot ($T \sim 395$ K) aqueous solution ($c. \sim 10^{-3}$ M) to room temperature.

The apparatus used for the spectroscopic measurements at different temperatures and under magnetic fields has been described in refs. 20 and 21.

A single crystal of $[Pt(bpm)(CN)_2]\cdot H_2O$ (approx. dimensions 0.06 × 0.06 × 0.12 mm) was used for data collection on a Enraf-Nonius CAD-4 diffractometer (Mo Kα, λ = 0.71073 Å, graphite monochromator in incident beam). Lattice parameters were refined from 2θ values of 25 reflections in the range $7.8 \leqslant \theta \leqslant 12.6°$. Intensities were measured for $2 \leqslant \theta \leqslant 28°$ in an ω–2θ scan technique, scan width $(0.7 + 0.34 \tan\theta)°$. ψ scans showed serious absorption effects. Three standard reflections showed no loss of intensity throughout data collection. Merging of the 5646 collected inten-

*Authors to whom correspondence should be addressed.

0020-1693/90/$3.50

sities ($\sin\theta_{max}/\lambda = 0.66$ Å^{-1}; $-9 \leqslant h \leqslant 9$, $-11 \leqslant k \leqslant 11$, $0 \leqslant l \leqslant 23$) gave 2743 unique reflexions with $I > 2\sigma(I)$ ($R_{int} = 0.023$) which were considered as observed and used for all subsequent calculations.

The structure was solved by Patterson and direct methods using the program SHELXS-86, followed by successive Fourier and difference Fourier syntheses (program system SDP 3.0; Enraf-Nonius). In full-matrix least-squares refinement $|F|$ magnitudes were used to refine atomic coordinates and temperature factors of the non-hydrogen atoms. After convergence at $R_w = 0.039$ (73 variables) a numerical correction for absorption was applied (program DIFABS; $T_{min} = 0.82$, $T_{max} = 0.99$). Final residuals after anisotropic refinement (163 variables) $R = 0.066$, $R_w = 0.037$, $w = 4I/(\sigma^2(I) + 0.04^2I^2)$, $S = 0.78$. Max. features in the final $\Delta\rho$ map ± 1.8 e Å^{-3}.

Results

Structure

The space group of $[Pt(bpm)(CN)_2]\cdot H_2O$ ($M = 423.4$) is $P2_1/c$ with $Z = 4$. The unit cell is characterized by the following parameters: $a = 7.076(1)$, $b = 8.999(2)$, $c = 18.127(2)$ Å, $\beta = 99.84(1)°$, $V = 1137.29$ Å^3 and $D_x = 2.47$ g cm^{-3}. In the complex molecule the surrounding of the platinum ion is planar, yielding the molecular point group C_{2v} (double group C'_{2v}), cf. Fig. 1. Figure 2 shows the

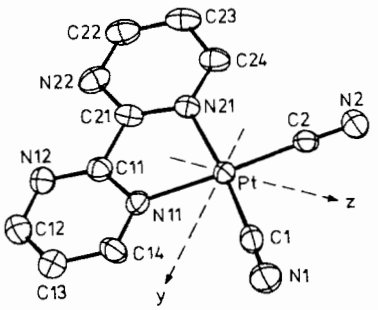

Fig. 1. ORTEP plot of the complex $[Pt(bpm)(CN)_2]$ (bpm = 2,2'-bipyrimidine) and the molecular axes ($x \perp y, z$). H atoms omitted.

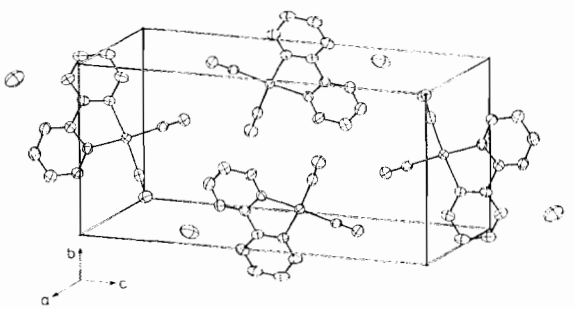

Fig. 2. ORTEP plot of the complexes $[Pt(bpm)(CN)_2]$ in the unit cell of $[Pt(bpm)(CN)_2]\cdot H_2O$. H atoms omitted.

TABLE 1. Positional parameters and their e.s.d.s for $[Pt(bpm)CN_2]\cdot H_2O$[a]

Atom	x	y	z	B (Å^2)
Pt	0.71469(4)	0.41304(3)	−0.00290(1)	2.001(4)
O	0.918(1)	0.6536(9)	0.3543(4)	5.9(2)
N1	0.795(1)	0.5295(8)	−0.1553(4)	3.7(2)
N2	0.617(1)	0.1044(9)	−0.0751(4)	4.5(2)
N11	0.7798(8)	0.6072(7)	0.0569(3)	2.4(1)
N12	0.806(1)	0.7048(8)	0.1800(4)	3.3(1)
N21	0.6735(8)	0.3444(7)	0.1006(3)	2.4(1)
N22	0.703(1)	0.4295(8)	0.2265(3)	3.3(1)
C1	0.762(1)	0.4869(9)	−0.0993(4)	2.6(2)
C2	0.655(1)	0.219(1)	−0.0498(4)	2.9(2)
C11	0.771(1)	0.5963(9)	0.1295(4)	2.6(1)
C12	0.857(1)	0.837(1)	0.1531(5)	3.5(2)
C13	0.873(1)	0.860(1)	0.0794(6)	3.8(2)
C14	0.834(1)	0.738(1)	0.0316(5)	3.1(2)
C21	0.712(1)	0.4485(8)	0.1559(4)	2.5(2)
C22	0.640(1)	0.293(1)	0.2457(5)	3.9(2)
C23	0.591(1)	0.182(1)	0.1928(5)	3.5(2)
C24	0.610(1)	0.2094(9)	0.1190(4)	2.9(2)

[a]H atoms omitted. Anisotropically refined atoms are given in the form of the isotropic equivalent displacement parameter defined as: $4/3\,\Sigma_i\Sigma_j\beta_{ij}\,a_i\cdot a_j$.

TABLE 2. Selected bond distances (Å) of $[Pt(bpm)(CN)_2]\cdot H_2O$[a]

Atom 1	Atom 2	Distance
Pt	N11	2.066(8)
Pt	N21	2.043(7)
Pt	C1	1.952(9)
Pt	C2	1.95(2)
N1	C1	1.14(1)
N2	C2	1.14(1)
N11	C11	1.33(2)
N11	C14	1.34(1)
N12	C11	1.33(1)
N12	C12	1.36(1)
N21	C21	1.36(1)
N21	C24	1.36(1)
N22	C21	1.30(2)
N22	C22	1.38(1)
C11	C21	1.50(1)
C12	C13	1.38(2)
C13	C14	1.40(1)
C22	C23	1.39(1)
C23	C24	1.39(1)

[a]Numbers in parentheses are e.s.d.s in the last significant digits.

unit cell with the four $[Pt(bpm)(CN)_2]$ complexes and oxygen atoms. In Tables 1–3, the positional parameters, the interatomic distances (Å), and the bond angles (°), respectively, are given. The planes of the complexes are inclined to the *bc*-plane by an angle of 28°. The Pt atoms form zigzag chains with

TABLE 3. Selected bond angles (°) for $[Pt(bpm)(CN)_2]\cdot H_2O$[a]

Atom 1	Atom 2	Atom 3	Angle
N11	Pt	N21	80.1(3)
N11	Pt	C1	97.3(3)
N11	Pt	C2	174.2(4)
N21	Pt	C1	177.1(3)
N21	Pt	C2	94.3(3)
C1	Pt	C2	88.4(4)
Pt	N11	C11	114.4(6)
Pt	N11	C14	127.9(6)
C11	N11	C14	117.9(8)
C11	N12	C12	115.3(9)
Pt	N21	C21	115.1(6)
Pt	N21	C24	127.0(7)
C21	N21	C24	117.9(7)
C21	N22	C22	116.0(8)
Pt	C1	N1	178.2(8)
Pt	C2	N2	177.7(9)
N11	C11	N12	126.1(9)
N11	C11	C21	116.3(8)
N12	C11	C21	117.5(8)
N12	C12	C13	123.3(9)
C12	C13	C14	116.4(9)
N11	C14	C13	121(1)
N21	C21	N22	126.5(8)
N21	C21	C11	114.1(7)
N22	C21	C11	119.5(9)
N22	C22	C23	121.8(9)
C22	C23	C24	119(1)
N21	C24	C23	119.2(9)

[a]Numbers in parentheses are e.s.d.s in the last significant digits.

alternating distances of 3.435(1) and 4.315 Å. The chains are parallel both with the crystallographic *a* axis and with the needle axis of the single crystal. Neighboring complexes of the same chain are mutually rotated by 180°.

Absorption

Figure 3 shows the **E** ∥ **a** polarized absorption spectrum of single crystal $[Pt(bpm)(CN)_2]\cdot H_2O$ at T = 10 K. Between $\bar{\nu}$ = 22 600 and 24 500 cm^{-1} the spectrum exhibits a distinct structure composed of five bands labelled by A–E. The low energy band A has an extinction coefficient of $\epsilon_{\parallel} \sim 130$ M^{-1} cm^{-1} and is separated from the bands B, C, D, E by $\Delta\bar{\nu}$ = 356, 763, 1002 and 1514 (±30) cm^{-1}, respectively. At $\bar{\nu} \gtrsim 24\,500$ cm^{-1} the extinction increases strongly. The **E** ⊥ **a** polarized absorption spectrum has the same shape as the **E** ∥ **a** spectrum, the extinction, however, is lower by a factor of about 3.5.

With decreasing temperature the absorption spectra display a rich fine structure, as shown in Fig. 4 for **E** ⊥ **a** polarization at T = 1.9 K. The fine structure lines have half-widths of $\Delta\bar{\nu}_{1/2} \sim 3$ cm^{-1}.

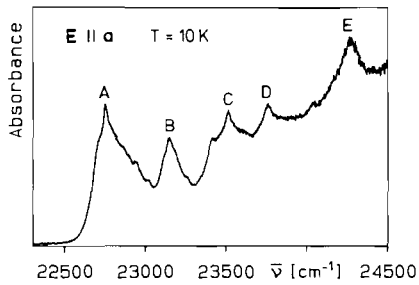

Fig. 3. E ∥ a polarized absorption spectrum of single crystal $[Pt(bpm)(CN)_2]\cdot H_2O$ at T = 10 K. Thickness of the crystal about 20 μm.

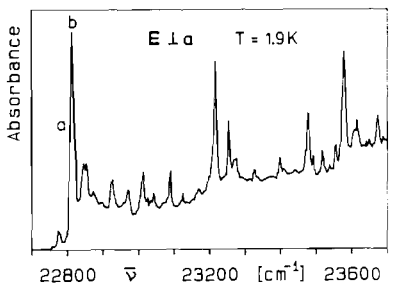

Fig. 4. E ⊥ a polarized absorption spectrum of single crystal $[Pt(bpm)(CN)_2]\cdot H_2O$ at T = 1.9 K. Thickness of the crystal about 10 μm.

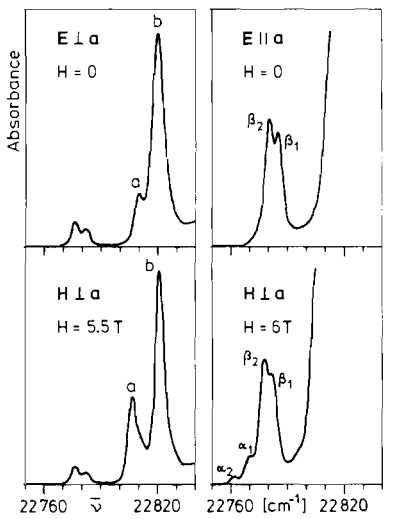

Fig. 5. Low energy section of the polarized absorption spectra of single crystal $[Pt(bpm)(CN)_2]\cdot H_2O$ at zero magnetic field (upper part) and at H = 6 T (lower part). T = 1.9 K. Thickness of the crystal about 10 μm.

In the upper part of Fig. 5 the low energy sections of the **E** ∥ **a** and the **E** ⊥ **a** polarized spectra are given on a larger scale. For **E** ⊥ **a** two strong bands a and b at $\bar{\nu}$ = 22 809 and 22 820 cm^{-1}, respectively, and an additional weak absorption at $\bar{\nu} \sim 22\,780$ cm^{-1} are observed. In the **E** ∥ **a** spectrum this weak absorption has a distinctly stronger extinction than for

$\mathbf{E} \perp \mathbf{a}$ polarization and can be resolved as a pair of lines β_1 and β_2 at $\bar{\nu}$ = 22 782 and 22 777 cm^{-1}, respectively.

Homogeneous magnetic fields **H** affect the low energy absorption lines considerably, independent of the orientation ($\mathbf{H} \parallel \mathbf{a}$ or $\mathbf{H} \perp \mathbf{a}$) of the fields, cf. the lower part of Fig. 5. At T = 1.9 K the lines a and b of the $\mathbf{E} \perp \mathbf{a}$ polarized spectrum are shifted by $\Delta\bar{\nu} \sim -2.9$ and +2.1 cm^{-1}, respectively, if the magnetic field strength is raised to H = 6 T. Simultaneously their extinction increases slightly and a shoulder at $\bar{\nu}$ = 22 815 cm^{-1} appears. In the $\mathbf{E} \parallel \mathbf{a}$ polarized spectrum the low energy flank of the strong absorption at $\bar{\nu}$ = 22 810 cm^{-1} is red shifted by ~6 cm^{-1} at H = 6 T, whereas the lines β_1 and β_2 show no magnetic field effects. At $< \mathbf{H} \geqslant$ T, however, additional very weak bands α_1 and α_2 at $\bar{\nu}$ = 22 770 and 22 764 cm^{-1}, respectively, and a shoulder at $\bar{\nu}$ = 22 795 cm^{-1} occur.

Emission

The $\mathbf{E} \parallel \mathbf{a}$ and $\mathbf{E} \perp \mathbf{a}$ polarized emission spectra of single crystal $[Pt(bpm)(CN)_2] \cdot H_2O$ at T = 1.9 K exhibit similar features and are distinctly structured by lines of half-widths of about 2 cm^{-1}, cf. Figs. 6 and 7, respectively. The $\mathbf{E} \parallel \mathbf{a}$ spectrum, however, displays several additional relatively intense lines labelled by asterisks. The difference between the two polarized spectra can be pointed out obviously in the high energy range of the emission, cf. Fig. 8. At T = 1.9 K both spectra show an intense line II at $\bar{\nu}$ = 22 766 cm^{-1}. For $\mathbf{E} \parallel \mathbf{a}$ polarization an additional intense line I ($\bar{\nu}$ = 22 776 cm^{-1}) has been observed. Similarly shaped pairs of lines with an energy separation of $\Delta\bar{\nu}$ = 10 cm^{-1} occur several times in the $\mathbf{E} \parallel \mathbf{a}$ spectrum at lower energies, e.g. the double peak III in Fig. 6. The high energy edge of the emission is formed by three very weak bands 1, 2, 3 ($\bar{\nu}$ = 22 820, 22 809, 22 795 cm^{-1}) whose intensities depend on the polarization.

Increase of the temperature from T = 1.9 to 5 K changes the emission spectra, as shown in Figs. 6, 7 and 8. Several lines disappear and at $T \sim 5$ K the spectra with $\mathbf{E} \parallel \mathbf{a}$ and $\mathbf{E} \perp \mathbf{a}$ polarization have nearly the same shape, they differ only by their intensities ($I_\parallel / I_\perp \sim 3$). Line I acquires intensity and at the blue flank of line I the weak band 1 grows up. Similar effects can be observed for the other double peaks of the $\mathbf{E} \parallel \mathbf{a}$ spectrum mentioned above.

Increase of the temperature from T = 5 to 10 K yields an additional drastical change of the spectra. Line 1 gains intensity and assumes a similar shape as line I at T = 5 K. In the $\mathbf{E} \parallel \mathbf{a}$ spectrum it becomes the dominating line. Simultaneously several addi-

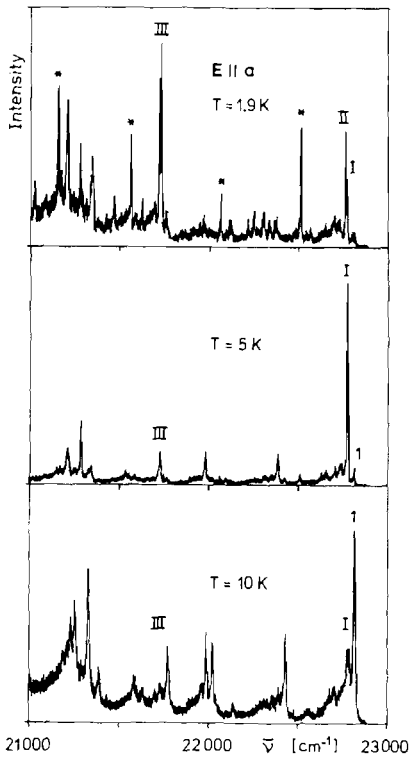

Fig. 6. $\mathbf{E} \parallel \mathbf{a}$ polarized emission spectrum of single crystal $[Pt(bpm)(CN)_2] \cdot H_2O$ at different temperatures. λ_{exc} = 364 nm.

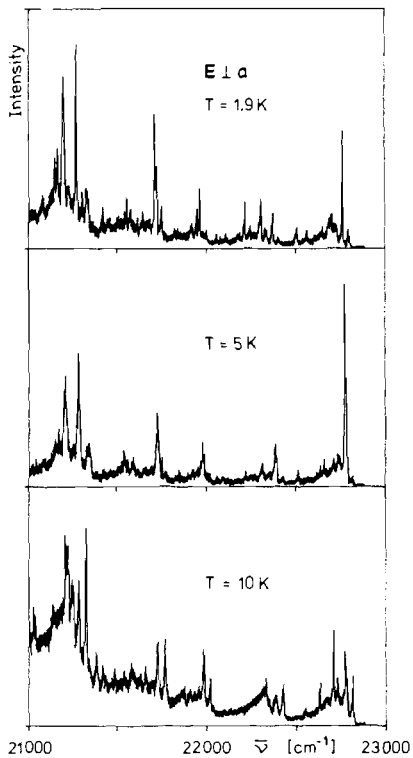

Fig. 7. $\mathbf{E} \perp \mathbf{a}$ polarized emission spectrum of single crystal $[Pt(bpm)(CN)_2] \cdot H_2O$ at different temperatures. λ_{exc} = 364 nm.

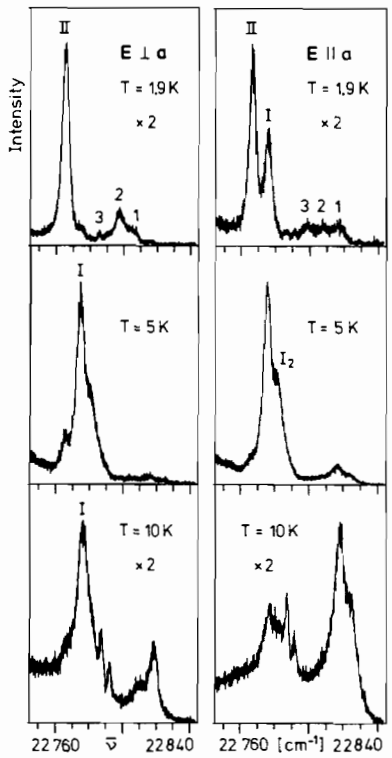

Fig. 8. High energy section of the polarized emission spectra of single crystal $[Pt(bpm)(CN)_2]\cdot H_2O$ at different temperatures. λ_{exc} = 364 nm.

tional lines appear in the lower energy range. Line 1 is the emission line of highest energy and is not changed perceptibly if the temperature is increased further to $T \sim 40$ K.

Between T = 1.9 and 5 K the total intensity of the **E** ∥ **a** emission increases by a factor of about 2. This yield is lost again if the temperature reaches T = 20 K. With further increase of the temperature the **E** ∥ **a** emission becomes weaker and at T = 120 K it is below the limit of detection. For **E** ⊥ **a** polarization the temperature induced reduction of the intensity is more pronounced and at $T \gtrsim 15$ K no **E** ⊥ **a** intensity is detectable.

The emission can be influenced by homogeneous magnetic fields **H**. For **H** ∥ **a** and **H** ⊥ **a** similar effects have been observed. Figures 9 and 10 show the high energy range of the **E** ∥ **a** and the **E** ⊥ **a** polarized spectra at T = 1.9 K, respectively, for H = 0 and 6 T with **H** ∥ **a**. The inserts display the high energy edges of the emission spectra on a larger scale. Under the magnetic field the spectra exhibit several conspicious features. The integral intensity increases, several lines grow drastically, other lines disappear, the spectral position of several lines is slightly shifted, and at H = 6 T the shapes of the differently polarized spectra coincide practically.

By a magnetic field strength H = 6 T the intensity of line II is increased by factors of 70 and 20 for

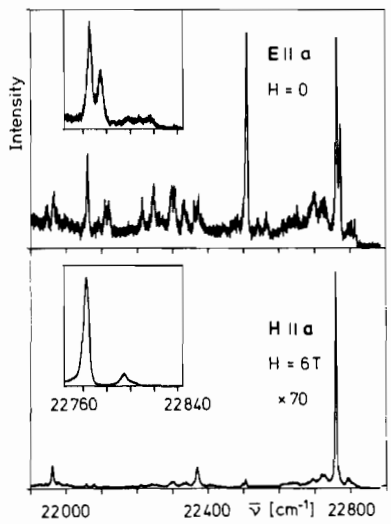

Fig. 9. E ∥ a polarized emission spectrum of single crystal $[Pt(bpm)(CN)_2]\cdot H_2O$ at H = 0 and H = 6 T with H ∥ a. T = 1.9 K. λ_{exc} = 364 nm. The inserts show the high energy section on a larger scale.

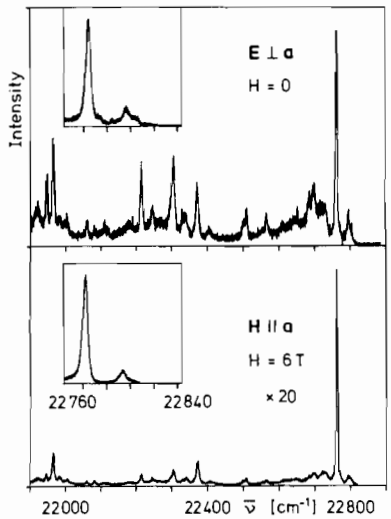

Fig. 10. E ⊥ a polarized emission spectrum of single crystal $[Pt(bpm)(CN)_2]\cdot H_2O$ at H = 0 and H = 6 T with H ∥ a. T = 1.9 K. λ_{exc} = 364 nm. The inserts show the high energy section on a larger scale.

E ∥ **a** and **E** ⊥ **a** polarization, respectively, and line I (in the **E** ∥ **a** spectrum) is deleted. A corresponding behavior has been observed for the above mentioned doublets (line separation $\Delta\bar{\nu} \sim 10$ cm^{-1}) at lower energies, e.g. the doublet III in Fig. 6. Applied magnetic fields shift line II to lower energies, independent of the polarization. This red shift is small at $H \leqslant 1$ T ($|\Delta\bar{\nu}| < 0.5$ cm^{-1}). It increases at $H > 1$ T and at H = 6 T it reaches the value $\Delta\bar{\nu} = -4$ cm^{-1} and no saturation of the shift is indicated. From the three peaks of highest energy, peak 3 acquires intensity and at $H \gtrsim 3$ T it is the dominating peak

of the triplet, both for $\mathbf{E} \parallel \mathbf{a}$ and for $\mathbf{E} \perp \mathbf{a}$ polarization.

For the orientation $\mathbf{H} \perp \mathbf{a}$ very similar magnetic field induced changes of the emission spectra have been observed. Only the increase of the intensity is distinctly lower. For example, the intensity of line II grows by factors of 15 and 5 for $\mathbf{E} \parallel \mathbf{a}$ and $\mathbf{E} \perp \mathbf{a}$ polarization, respectively, if the field strength H is raised to 6 T.

Discussion

As shown above the complex $[Pt(bpm)(CN)_2]$ has the symmetry C_{2v}, cf. Fig. 1. By a ligand field of C_{2v} symmetry the degeneracy of the platinum(II) 5d-states is partially removed according to the following energy order [16, 17, 22]: $a_1(x^2) < b_1(xz)$, $a_2(xy) < a_1(y^2 - z^2) \ll b_2(yz)$. The three 6p-states of the central ion also have different energies in the ligand field: $b_1(x) < b_2(y) \sim a_1(z)$. The LUMOs of the $(CN)_2$ system and of the 2,2′-bipyrimidine molecule are π^* states of symmetry b_1. The energies of these states are expected in the same range as that of the metal $6p_x$ state. Thus, all these b_1 states can mix, yielding the LUMO $b_1(x, \pi^*_{CN}, \pi^*_{bpm})$ of the complex. Correspondingly a hybrid of the π state $a_2(\pi_{bpm})$ of the 2,2′-bipyrimidine molecule and the metal 5d-state $a_2(xy)$ forms the HOMO of the complex.

With these MOs the ground electronic state $^1A_1$-$(1A_1')$ and the lowest excited electronic states $^3B_2$-$(2A_1', A_2', B_1')$ and $^1B_2(B_2')$ of the complex result. In the crystal, the excited states of the complexes form exciton bands, which are expected to be very small, because of the relatively large distance between neighboring complexes. A corresponding energy level diagram is shown at the left hand side of Fig. 11. The energy order of the triplet components has been chosen according to the experimental results, as will be shown below. Electric dipole transitions between the ground state and the excited singlet state are spin and symmetry allowed with polarization $\mathbf{E} \parallel \mathbf{y}$. Via spin–orbit coupling additional transitions between the ground state and the triplet components $2A_1'$ and B_1' are $\mathbf{E} \parallel \mathbf{z}$ and $\mathbf{E} \parallel \mathbf{x}$, respectively, allowed. Electric dipole transitions between the ground state and the triplet component A_2', however, are both symmetry and spin forbidden.

A conspicuous feature of the spectra is the energetic overlap of the absorption and the emission, cf. Figs. 5 and 8. For example the emission bands I and II coincide energetically with the weak absorption lines β_2 and α_2, respectively, and the absorption bands a and b have the same energies as the emission lines 2 and 1, respectively. This energetic overlap and the behavior of the peaks inside that range of overlap at varying temperature and at

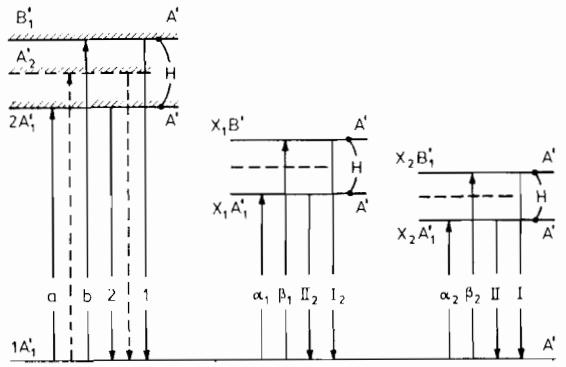

Fig. 11. Schematic diagram of the lowest electronic energy levels of single crystal $[Pt(bpm)(CN)_2]\cdot H_2O$. The labels at the left ends of the levels belong to the zero field case (symmetry C_{2v}), those at the right ends to $H \neq 0$ with $\mathbf{H} \perp \mathbf{a}$ (symmetry C_1).

applied magnetic fields suggest the existence of two types of X traps, X_1 and X_2. These traps appertain to complexes, which are slightly disturbed by impurities or lattice defects. They have sharp energy levels arranged below the corresponding exciton bands, as shown at the right hand side of Fig. 11.

The absorption between $\bar{\nu} = 22\,820$ and $\sim 24\,000$ cm^{-1}, as presented in Fig. 3, can be assigned to the $\mathbf{E} \parallel \mathbf{x}$ polarized singlet–triplet transition between the ground state $1A_1'$ and the exciton band B_1' and to accompanying vibrational satellites. The observed ratio of the extinction coefficients $\epsilon_{\parallel a}$ and $\epsilon_{\perp a}$, $\epsilon_{\parallel a}/\epsilon_{\perp a} \sim 3$–4, is in accordance with the angle of 28° between the crystallographic axis a and the molecular axis x. The maximum value of $\epsilon_{\parallel a}$ (~ 130 M^{-1} cm^{-1}) corresponds to $\epsilon_{\parallel x} \sim 170$ M^{-1} cm^{-1}. This relatively large value of the extinction coefficient can be explained by two factors. First, both the HOMO and the LUMO of the complex contain admixtures of Pt wavefunctions. Second, the B_1' state can acquire partly singlet character by spin–orbit coupling with the singlet $^1B_1[a_1(y^2 - z^2) \rightarrow b_1(x, \pi^*_{CN}, \pi^*_{bpm})]$.

More insight into the absorption processes results from the low energy section of the 1.9 K spectra. The bands b and a in the $\mathbf{E} \perp \mathbf{a}$ polarized spectrum (cf. Fig. 4 and the left hand side of Fig. 5) can be assigned to the 0–0-transitions from the ground state $1A_1'$ to the exciton bands $B_1'(\mathbf{E} \parallel \mathbf{x})$ and $2A_1'(\mathbf{E} \parallel \mathbf{z})$, respectively. The ratio of the observed extinction coefficients of the two bands, $\epsilon_{\perp a}$ (band b)/$\epsilon_{\perp a}$(band a) ~ 5, yields the ratio $\epsilon_{\parallel x}$(band b)/$\epsilon_{\parallel z}$(band a) ~ 18. Thus, in the $\mathbf{E} \parallel \mathbf{a}$ spectrum the extinction of the transition $1A_1' \rightarrow 2A_1'$ is by a factor of <0.1 smaller than that of the transiton $1A_1' \rightarrow B_1'$.

The weak absorption peaks β_1 and β_2 (cf. Fig. 4 and the upper part of Fig. 5) are assigned to 0–0 transitions from the ground state $1A_1'$ to the X-trap

states X_1B_1' and X_2B_1', respectively. Because of their distinctly lower probabilities the transitions $1A_1' \rightarrow X_1A_1'$ and $1A_1' \rightarrow X_2A_1'$ are below the limit of detection at $H = 0$. From the extinction coefficients of the peaks β_1 and β_2 the concentration of the X-traps can be estimated to ~5% of all complexes in the crystal. This concentration is distinctly higher than that observed in other systems, which contain X traps, too [7, 8]. In the latter systems the existence of X traps could not be proved directly by transmission spectroscopy as in our case but only indirectly by excitation spectroscopy.

Under a homogeneous magnetic field, $\mathbf{H} \perp \mathbf{a}$, the symmetry of the system is reduced from C_{2v} to C_1. All states transforming as A_1', A_2' and B_1' at C_{2v}, have the same symmetry A' at C_1 and can mix, indicated by the coupling symbols in Fig. 11. By this process the peaks a, α_1 and α_2, which can be assigned to the 0–0 transitions from the ground electronic state to the triplet components $2A_1'$, X_1A_1', X_2A_1', respectively, acquire extinction from the relatively strong peaks b, β_1, and β_2, respectively, as shown in the lower part of Fig. 5. This assignment is confirmed by the fact, that the energy differences between the peaks α_2 and β_2, between α_1 and β_1, and between a and b have the same value $\Delta\bar{\nu} = 10 \pm 2$ cm^{-1}. The very weak shoulder ($\bar{\nu} \sim$ 22815 cm^{-1}) between the bands a and b belongs probably to the transition $A'(1A_1') \rightarrow A'(A_2')$. The magnetic field induced shift of the peaks a and b by $\Delta\bar{\nu} \sim -2.9$ cm^{-1} and +2.1 cm^{-1}, respectively, at $H = 6$ T is due to the Zeeman repulsion of the levels B_1' and $2A_1'$.

The emission spectra result from radiative deactivations of the traps X_1 and X_2 and of the exciton bands, and from accompanying vibrational and phonon satellites. After the excitation of the crystal the exciton bands of $^3B_2$ parentage are populated by a radiationless relaxation. The energy propagating within the exciton bands can be emitted as a photon or be trapped by the X traps. At low temperatures the trapping rates are expected to be distinctly larger than the rates of the detrapping processes (from the traps X_1, X_2 to the exciton bands). Because of the relatively high trap concentration a direct energy transfer between the traps cannot be precluded. Therefore, the total energy transfer between the traps follows this direct mechanism or the route via the exciton bands.

At $T = 1.9$ K the emission is mainly due to the radiative deactivation of the low energy states X_2A_1' and X_2B_1', yielding the emission peaks II and I, cf. Fig. 8. The electric dipole transitions $X_2A_1' \rightarrow 1A_1'$ and $X_2B_1' \rightarrow 1A_1'$ are $\mathbf{E} \parallel z$ and $\mathbf{E} \parallel x$ polarized, respectively. Regarding the angle of 28° between the axes a and x, intensity ratios $I_{\parallel a}/I_{\perp a}$ of 3.5 and 0.3 for the peaks I and II, respectively, are expected. These values are confirmed roughly by the experimental data. The peaks 1 and 2 can be assigned to 0–0 emission processes, which start from the exciton bands B_1' and $2A_1'$, respectively. This assignment agrees with the polarization properties and with the energies of the corresponding absorption bands. The energies of the X_1 states are higher by $\Delta\bar{\nu} \sim 5$ cm^{-1} than the corresponding X_2 states. At $T = 1.9$ K the intensities of the transitions $X_1A_1' \rightarrow 1A_1'$ and $X_1B_1' \rightarrow 1A_1'$ will be distinctly lower than those of the bands II and 1, respectively. Thus, the emission peaks due to the X_1 traps are hidden below the flanks of the bands II and I.

With increasing temperature the state X_2B_1' becomes more and more thermally populated. Since this state has a distinctly higher radiative transition probability to the ground electronic state than the state X_2A_1', the intensity of band II decreases and the emission band I grows, cf. Fig. 8. At $T \sim 5$ K a shoulder at the high energy flank of band I appears. It can be assigned to the transition $X_1B_1' \rightarrow 1A_1'$, which acquires intensity by the thermal increase of the population of state X_1B_1'.

At further increase of the temperature to $T \sim 10$ K the emission from the states of B_1' symmetry dominates (bands I, I_2, 1). The peaks at $\bar{\nu} = 22785$ and 22790 cm^{-1} and the double structure of band 1 can not be explained conclusively. Possibly these features are due to phonon coupling.

The effect of applied homogeneous magnetic fields $\mathbf{H} \perp \mathbf{a}$ on the emission spectra can be discussed straightforwardly on the basis of the energy level scheme of Fig. 11. At high magnetic field strengths, $3 \text{ T} \lesssim H \lesssim 6$ T, the 1.9 K emission is owing mainly to the radiative deactivation of the excited states $A'(X_2A_1')$ and $A'(2A_1')$. Compared with the zero field case the corresponding bands II and 2 are red shifted because of the Zeeman repulsion by the states $A'(X_2B_1')$ and $A'(B_1')$, respectively. The intensity increase of the bands II and 2 is due to admixtures of B_1' components, which yield a large probability of electric dipole transitions to the ground electronic state. Since in the symmetry C_1 the transitions $A' \rightarrow A'$ are non-polarized, the emission spectra at $H = 6$ T are independent of the polarization.

Supplementary Material

Tables containing values of F_0 and F_2, anisotropic thermal parameters, and a complete list of atomic distances and bond angles can be obtained upon request from the authors.

Acknowledgements

This research has been supported by the Deutsche Forschungsgemeinschaft and the Fonds der Chemischen Industrie.

References

1 S. Sprouse, K. A. King and R. J. Watts, *J. Am. Chem. Soc., 106* (1984) 6647.
2 Y. Ohsawa, S. Sprouse, K. A. King, M. K. DeArmond, K. W. Hank and R. J. Watts, *J. Phys. Chem., 91* (1987) 1047.
3 M. Maestri, D. Sandrini, V. Balzani, U. Maeder and A. v. Zelewsky, *Inorg. Chem., 26* (1987) 1323.
4 U. Maeder, T. Jenny and A. v. Zelewsky, *Helv. Chim. Acta, 69* (1986) 1085.
5 S. Bonafede, M. Ciano, F. Bolletta, V. Balzani, L. Chassot and A. v. Zelewsky, *J. Phys. Chem., 90* (1986) 3836.
6 C. Cornioley-Deuschel and A. v. Zelewsky, *Inorg. Chem., 26* (1987) 3354.
7 R. Schwarz, G. Gliemann, Ph. Jolliet and A. v. Zelewsky, *Inorg. Chem., 28* (1989) 742.
8 R. Schwarz, G. Gliemann, Ph. Jolliet and A. v. Zelewsky, *Inorg. Chem., 28* (1989) 1053.
9 L. Bär, G. Gliemann, L. Chassot and A. v. Zelewsky, *Chem. Phys. Lett., 123* (1986) 264.
10 L. Chassot, E. Müller and A. v. Zelewsky, *Inorg. Chem., 23* (1984) 4249.
11 V. Balzani, F. Bolletta, M. T. Gandolfi and M. Maestri, *Top. Curr. Chem., 75* (1978) 1.
12 G. A. Crosby, *Acc. Chem. Res., 8* (1975) 231.
13 G. A. Crosby, *J. Chem. Educ., 60* (1983) 791.
14 R. J. Watts, G. A. Crosby and J. L. Sansegret, *Inorg. Chem., 11* (1972) 1474.
15 R. J. Watts and G. A. Crosby, *Chem. Phys. Lett., 13* (1972) 619.
16 R. Schwarz, M. Lindner and G. Gliemann, *Ber. Bunsenges. Phys. Chem., 91* (1987) 1233.
17 J. Biedermann, M. Wallfahrer and G. Gliemann, *J. Lumin., 37* (1987) 323.
18 J. Biedermann, G. Gliemann, U. Klement, K.-J. Range and M. Zabel, to be published.
19 P. M. Kiernan and A. Ludi, *J. Chem. Soc., Dalton Trans.,* (1978) 1127.
20 J. Hidvegi, W. v. Ammon and G. Gliemann, *J. Chem. Phys., 76* (1982) 4361.
21 W. Tuszynski and G. Gliemann, *Ber. Bunsenges. Phys. Chem., 89* (1985) 940.
22 M. Textor and H. R. Oswald, *Z. Anorg. Allg. Chem., 407* (1974) 244.